frontiers in Chemistry

ORIGINAL RESEARCH
published: 29 September 2021
doi: 10.3389/fchem.2021.754487

All-Inorganic p–n Heterojunction Solar Cells by Solution Combustion Synthesis Using N-type $FeMnO_3$ Perovskite Photoactive Layer

Ioannis T. Papadas[1,2], Apostolos Ioakeimidis[1], Ioannis Vamvasakis[3], Polyvios Eleftheriou[1], Gerasimos S. Armatas[3] and Stelios A. Choulis[1]**

[1]Molecular Electronics and Photonics Research Unit, Department of Mechanical Engineering and Materials Science and Engineering, Cyprus University of Technology, Limassol, Cyprus, [2]Department of Public and Community Health, School of Public Health, University of West Attica, Athens, Greece, [3]Department of Materials Science and Technology, University of Crete, Heraklion, Greece

OPEN ACCESS

Edited by:
Konstantinos Christoforidis, Democritus University of Thrace, Greece

Reviewed by:
Dimitris Tsikritzis, Hellenic Mediterranean University, Greece
Dimitris A. Chalkias, University of Peloponnese, Greece

***Correspondence:**
Ioannis T. Papadas
ioannis.papadas@cut.ac.cy
Stelios A. Choulis
stelios.choulis@cut.ac.cy

Specialty section:
This article was submitted to Nanoscience, a section of the journal Frontiers in Chemistry

Received: 06 August 2021
Accepted: 13 September 2021
Published: 29 September 2021

Citation:
Papadas IT, Ioakeimidis A, Vamvasakis I, Eleftheriou P, Armatas GS and Choulis SA (2021) All-Inorganic p–n Heterojunction Solar Cells by Solution Combustion Synthesis Using N-type $FeMnO_3$ Perovskite Photoactive Layer. Front. Chem. 9:754487. doi: 10.3389/fchem.2021.754487

This study outlines the synthesis and physicochemical characteristics of a solution-processable iron manganite ($FeMnO_3$) nanoparticles via a chemical combustion method using tartaric acid as a fuel whilst demonstrating the performance of this material as a n-type photoactive layer in all-oxide solar cells. It is shown that the solution combustion synthesis (SCS) method enables the formation of pure crystal phase $FeMnO_3$ with controllable particle size. XRD pattern and morphology images from TEM confirm the purity of $FeMnO_3$ phase and the relatively small crystallite size (~13 nm), firstly reported in the literature. Moreover, to assemble a network of connected $FeMnO_3$ nanoparticles, β-alanine was used as a capping agent and dimethylformamide (DMF) as a polar aprotic solvent for the colloidal dispersion of $FeMnO_3$ NPs. This procedure yields a ~500 nm thick $FeMnO_3$ n-type photoactive layer. The proposed method is crucial to obtain functional solution processed NiO/$FeMnO_3$ heterojunction inorganic photovoltaics. Photovoltaic performance and solar cell device limitations of the NiO/$FeMnO_3$-based heterojunction solar cells are presented.

Keywords: inorganic perovskites, solution combustion synthesis, FeMnO3, NiO, p-n junction, functional metal oxides, inorganic solar cells, photoactive nanomaterials

INTRODUCTION

A major source of renewable energy is solar energy (Ellabban et al., 2014). Nevertheless, the production of fuels and electricity from solar power is still costly, mainly because of the materials used in building the cells (Ellabban et al., 2014; Hussein, 2015). Except for Si and copper indium gallium selenide solar cells (CIGSSe), which are principal targets for photovoltaic (PV) applications, CdTe and GaAs are also significant photoactive materials. However, the mass production of such photovoltaics is limited due to the high production costs, the indirect bandgap energy (for Si) and the dependence on elements which are expensive (In, Ga, Te) or even hazardous (As, Cd) (Rohatgi, 1996; Mitzi et al., 2011; Kosten et al., 2013; Wang, 2014). Contrarily, hybrid lead halide perovskite solar cells (PVSCs) have been in the epicenter of the current solar cell research because of their facile fabrication process and due to the fact that they appear a high PCE of over 23% (Jung et al., 2019). However, PVSCs have disadvantages as well, that is, ultraviolet light absorption, and humidity and

atmospheric oxygen affecting decomposition (Li and Liu, 2017; Fu et al., 2018387). Along with the presence of toxic lead, these factors restrain the advancement of the PVSCs. Therefore, it is essential to find alternatives for inorganic PVs that use inexpensive, eco-friendly and Earth abundant photoactive materials with appropriate semiconductor structure, while at the same time seek improvements in solar cell efficiency.

Metal oxide (MeOx) based solar cells have the potential to resolve some of the issues which arise in conventional solar cells. The all-oxide perspective is advantageous due to its excellent chemical stability, minor toxicity and ample quantities of metal oxides that effectively permit the manufacturing of solar cells under ambient conditions (Pérez-Tomás et al., 2018). MeOx are typically used as functional layers in solar cells such as transparent conducting front electrodes (ITO, FTO), (Kim et al., 1999; Han et al., 2007) electron (TiO_2, SnO_2, ZnO, Fe_2O_3 etc.) (Seo et al., 2018; Xiong et al., 2018; Shin et al., 2019; Papadas et al., 2019) or hole (Cu:NiOx, $CuGaO_2$, $NiCo_2O_4$, CuLi:$NiCo_2O_4$ etc.) transporting layers, (Galatopoulos et al., 2017; Papadas et al., 2018a; Papadas et al., 2018b; Ioakeimidis et al., 2019) whereas a very small number of MeOx have been used as photoactive layers, primarily Cu_2O, CuO and Co_2O_3 (Pérez-Tomás et al., 2018).

Ferroic semiconductors are now being continually included in the list of materials which are employed to investigate and push the efficiency limits in all-oxide photovoltaics. Ferroic semiconductor materials are considered to be light absorbers, such as $Pb(Zr,Ti)O_3$ (energy band gap (E_g) = 3.63 eV) (Pérez-Tomas et al., 2019), $KNbO_3$ (E_g = 3.8 eV) (Grinberg et al., 2013) and $BiFeO_3$ (E_g = 2.67 eV) (Papadas et al., 2015a). However, what seems to confine their implication to solar cells is their wide energy bandgap that results to low absorption of visible light and, thus, low conductivity. Other ferroelectric oxide semiconductors, like Bi_2FeCrO_6 (Nechache et al., 2014) and $BiMnO_3$ (Sun et al., 2017), have a suitable bandgap between 1 and 2 eV and are considered as more efficient in absorbing solar light. It is worth mentioning that a power conversion efficiency (PCE) up to ~8.1% has been recently achieved using a single ferroelectric Bi_2FeCrO_6 layer fabricated by pulse laser deposited technique with the following structure: $SrTiO_3/SrRuO_3/Bi_2CrFeO_6$/ITO (Nechache et al., 2014). However, without the mentioned method of the thin film deposition which is considered to be a very complicated and energy demanding procedure, it is very unlikely to gain high PCE values (Calnan, 2014). Furthermore, the usage of the low-bandgap $KBiFe_2O_5$ material (E_g ~1.6 eV) in the photovoltaic cells appears to be restricted due to low PCE (~3 10^{-3}%) (Zhang et al., 2013). Therefore, the above mentioned examples demonstrate that further research is needed in finding more efficient narrow-bandgap, non-toxic and low-cost materials for solar cell devices.

The sol-gel synthesis has been the most frequently used method in the manufacture of MeOx. Nevertheless, to achieve crystallinity and to guarantee an efficient charge–carrier mobility, for metal oxide based active layers, high temperatures are necessary, which increases the cost of manufacturing and also restricts printable applications. These restrictions call for alternative techniques which could operate at lower temperatures. Compared to sol-gel synthesis of MeOx nanoparticles (NPs), the solution combustion synthesis (SCS) of NPs displays considerable advantages, such as use of a simple experimental setup, production of NPs with high crystallinity and pure phase, and exact control of the size and crystal structure of the particles by simple adjusting the fabrication conditions. (Suresh et al., 1991; Mimani and Patil, 2001; Patil et al., 2002a; Bansal, 2005; Deganello et al., 2009; Jadhav et al., 2011; Jiang et al., 2014) The SCS seems to be adaptable and effective for the growth of high crystalline MeOx layers at relative lower temperatures. As an exothermic procedure with a high rate of heat release, the necessity for high temperatures is circumvented and high purity MeOx NPs can be produced at moderate reaction conditions. In SCS process, the metal salts (e.g., nitrates) dissolved in saturated aqueous or alcoholic solutions act as oxidizing agents and react with organic fuels (such as urea, glycine, acetylacetonate, citric acid etc.) under relatively lower temperatures compared to other commonly used solution process methods to give rise to a combustion reaction and to produce the corresponding metal oxide NPs (Kim et al., 2011; Hsieh, 2014; Yu, 2015).

Iron manganite ($FeMnO_3$, FMO) is a mixed perovskite material with the chemical formula ABO_3, where the Fe atom is placed at the center of a cube formed by eight corner-sharing MnO_6 octahedra (Habibi and Mosavi, 2017). $FeMnO_3$ has been examined for applications such as lithium-ion batteries, catalysis, humidity sensors, energy storage and antibacterial devices (Doroftei et al., 2014; Cao et al., 2016; Cetin et al., 2019; Vasiljevic et al., 2020a; Nikolic et al., 2020). A large number of synthesis methods, such as co-precipitation, hydrothermal, ball milling, solid state reaction and sol-gel chemistry, have all been employed for the fabrication of $FeMnO_3$ materials (Sundari et al., 2013; Doroftei et al., 2014; Cao et al., 2016; Soni and Pal, 2016; Bin et al., 2017; Mungse et al., 2017; Gowreesan and Ruban Kumar, 2017; Saravanakumar et al., 2018; Cetin et al., 2019; Fix, 2019; Lobo and Rubankumar, 2019; Vasiljevic et al., 2020a; Nikolic et al., 2020; Vasiljevic et al., 2020b). Despite this, not all these techniques are viable to synthesize $FeMnO_3$ nanomaterials, as there are some drawbacks such as the expense of the source materials, chemical non-uniformity, high impurity, aggregated nanoparticles, and non-stoichiometry of some ferrite systems (Buonsanti et al., 2012; Alves et al., 2013; Bennet et al., 2016; Skliri, 2018). $FeMnO_3$ is a semiconductor which consists of plentiful and environmentally friendly elements with an ideal direct optical bandgap (~1.5 eV) to absorb solar photons, while it has a deep lying valence band (VB ~ 5.3 eV) (Skliri, 2018) that corresponds well to the VB edges of several p-type materials (e.g., CuO, $NiCo_2O_4$ etc.) (Savva et al., 2017; Papadas et al., 2018b). Additionally, it has high photochemical stability which is necessary for long-term optoelectronic devices while furthermore its intrinsic electric polarization field can enable charge-carrier separation within the semiconducting structure. Such characteristics make $FeMnO_3$ a promising light absorber for optoelectronic uses. On the other hand, between the numerous metal oxides that have been used as p-type active layers, nickel oxide (NiO) is a promising candidate for PVs due to its excellent electrochemical behavior (Kerli and Alver, 2016). NiO demonstrates a rock salt structure and exhibits adequate

p-type conductivity with a wide bandgap in the range of 3.5 eV (Chrissanthopoulos et al., 2011; Mahmood et al., 2011; Zhang, 2015). NiO has been reported as p-type material in all-oxide solar cells in combination with the n-type TiO_2 and ZnO materials, while also solution combustion synthesized NiOx is commonly used as HTL in perovskite solar cells (Warasawa et al., 2013; Kawade et al., 2015; Kerli and Alver, 2016; Karsthof et al., 2016; Galatopoulos et al., 2017; Patel, 2017; Ukoba et al., 2018).

In this work, SCS of $FeMnO_3$ NPs is presented while indicating that tartaric acid can be used as a fuel and nitrate as an oxidizer agent. $FeMnO_3$ NPs characterized by an average size of ~13 nm and a narrow particle-size distribution, were prepared using a low cost SCS process (6 h calcination at 450°C in air). The as-synthesized $FeMnO_3$ NPs were then functionalized with β-alanine and the ligand-capped NPs enabled the formation of compact and functional layers. These films were used, for the first time, as n-type photoactive materials and were incorporated in p-n heterojunction of all-oxide solar cells. For the purposes of this study, nanostructured NiO films were also synthesized by SCS method and applied as a p-type layer in the following structure ITO/NiO/$FeMnO_3$/Cu. The corresponding MeOx PVs show a high V_{oc} of 1.31 V with adequate FF of 54.3% and limited short current of 0.07 mA cm^{-2} resulting to a PCE of 0.05%. Electrical characterizations by impedance spectroscopy reveled a high charge recombination resistance inducing high V_{oc}, whereas the limited current density is ascribed to the high charge transport resistance. Despite the low PCE values, these results provide a framework for further optoelectronic properties research on eco-friendly and cost-effective photoactive layers for fabrication of all solution processable inorganic photovoltaics.

EXPERIMENTAL

Materials: Pre-patterned glass-ITO substrates (sheet resistance 4 Ω/sq) were purchased from Psiotec Ltd. All the other chemicals used in this study were purchased from Sigma Aldrich.

Solution combustion synthesis (SCS) of FeMn O_3 NPs: For the synthesis of $FeMnO_3$ NPs, 0.5 mmol $Mn(NO_3)_2.4H_2O$, 0.5 mmol $Fe(NO_3)_3.9H_2O$ and tartaric acid were blended in 5 ml of 2-methoxy ethanol solution. Subsequently, 150 µl HNO_3 (69% wt HNO_3) were added slowly into the mixture, and the solution stirred up to almost complete homogeneity. The whole solution was left under stirring for at least 3 h at room temperature (RT). The molar ratio of the total metal nitrates and tartaric acid was 1. Thereafter, the precursor solution was heated at 100°C under consecutive stirring until complete evaporation of the solvent. The dry black powder was then used for the combustion synthesis of the $FeMnO_3$ NPs in ambient atmosphere at 450°C in a preheated oven for 6 h, so that the combustion process be completed and then left to cool down at room temperature.

Perovskite FeMn O_3 films preparation: The prepared $FeMnO_3$ (FMO) NP powder was used for the preparation of FMO dispersion for the deposition of corresponding film by spin coating technique. Firstly, the surface of NPs was modified with β-alanine. Briefly, as-made FMO NPs (50 mg) were added in 4 ml of deionized (DI) water containing β-alanine (10 mg), and the pH of the solution was adjusted to 4.2 with 1M HNO_3. (Papadas et al., 2015b; Skliri, 2018) To secure that NPs will transfer to the liquid phase and form a stable suspension, typically within 1 day, the resulting mixture was then intensively stirred at RT. The dispersion was aided with probe sonicator for about 30 min. To a stable colloidal dispersion of 30 mg ml^{-1} be formed, the alanine-capped FMO NPs were isolated by centrifugation, rinsed several times with DI water, and finally dispersed in DMF. The obtained homogenous dispersion was then drop-casted and subsequently was spin coated on the top of NiO layer at 3,000 rpm for 40 s. The process of $FeMnO_3$ film formation was repeated about ten times to obtain a desired thickness of about 500 nm. To assemble a network of tightly connected metal oxide NPs, the deposition of the $FeMnO_3$ films was accomplished by spin coating technique of the colloidal NPs, followed by thermal annealing at 300°C for 30 min. In this way, β-alanine can enable direct NP–NP interactions upon ligand removal at growth temperature due to its small size, thus yielding high strength films consisted of firmly interconnected NP networks. This strategy is very important to obtain functional metal oxides photovoltaic devices with good charge transfer properties.

NiO NPs synthesis and films preparation by SCS: For the solution combustion synthesis of NiO, 1 mmol of $Ni(NO_3)_2{\cdot}6H_2O$ were dissolved in 2.5 ml of 2-methoxyethanol. After the solution was stirred at 50°C for 1 h, 0.1 mmol of acetylacetone was added to the solution, and the whole solution was allowed under further stirring for 1 h at RT. Spin coating technique was applied for the fabrication of the precursor films on the various substrates. The precursor's solution was spin coated at 3,000 rpm for 40 s. The resulting light green colored films were dried at 100°C for 5 min and used as a precursor for the combustion synthesis of NiO NPs. Subsequently the obtained films were heated at 300°C in ambient atmosphere for 1 h in a preheated hot plate to complete the combustion process and then left to cool down at room temperature, forming a ~50 nm thin layer.

Device fabrication: The metal oxides solar cells under study were ITO/NiO-NPs/$FeMnO_3$-NPs/Cu. ITO substrates were sonicated in acetone and subsequently in isopropanol for 10 min and then heated at 100°C on a hot plate for 10 min before use. The substrates were further treated with ozone for 10 min to achieve a better contact with the active layer by reducing the contact resistance. To fabricate the devices, a layer of NiO as p-type and $FeMnO_3$ as n-type side of the p-n junction were formed in sequence. The deposition of corresponding metal oxides films was described in detail above. Finally, 200 nm Cu layers were thermally evaporated through a shadow mask to finalize the devices, giving an active area of 0.9 mm^2.

Characterization: Thermogravimetric Analysis (TGA) were performed on a Shimadzu Simultaneous DTA-TG system (DTG-60H). Thermal analysis was conducted from 40 to 600°C in air atmosphere using air gas with a flow rate of 200 ml min^{-1} and a heating rate of 10°C min^{-1}. X-ray diffraction (XRD) patterns were collected on a PANanalytical X′pert Pro MPD powder diffractometer (40 kV, 45 mA) using Cu

Kα radiation (λ = 1.5418 Å). Transmission electron microscope (TEM) images and electron diffraction patterns were recorded on a JEOL JEM-2100 microscope with an acceleration voltage of 200 kV. The samples were first gently ground, suspended in ethanol, and then picked up on a carbon-coated Cu grid. Quantitative microprobe analyses were performed on a JEOL JSM-6390LV scanning electron microscope (SEM) equipped with an Oxford INCA PentaFET-x3 energy dispersive X-ray spectroscopy (EDS) detector. Data acquisition was performed with an accelerating voltage of 20 kV and 60 s accumulation time. Absorption measurements were performed with a Schimadzu UV-2700 UV-Vis spectrophotometer. For UV-VIS and PL measurements, thick films of $FeMnO_3$ NPs have been fabricated on top of the quartz substrates employing the spin coating method. UV–vis/near-IR diffuse reflectance spectra were recorded with a Schimadzu UV-2700 UV-Vis spectrophotometer, using $BaSO_4$ powder as a 100% reflectance standard. The energy bandgap (E_g) of the samples were estimated from Tauc plots of $(Fhv)^2$ as a function of photon energy (hv), where F is the Kubelka–Munk function of the reflectance (R): $F=(1-R)^2/(2R)$ (Kubelka, 1948). The thickness of the films were measured with a Veeco Dektak 150 profilometer. The PL measurements were performed on $FeMnO_3$ film on quartz substrate at an excitation wavelength of 400 nm. Photoluminescence (PL) spectrum was obtained at room temperature on a Jobin-Yvon Horiba FluoroMax-P (SPEX) spectrofluorimeter (Singapore) equipped with a 150 W Xenon lamp and operated from 300 to 900 nm. The current density-voltage (J-V) characteristics were characterized with a Botest LIV Functionality Test System. Forward bias scans were measured with 10 mV voltage steps and 40 msec of delay time. For illumination, a calibrated Newport Solar simulator equipped with a Xe lamp was used, providing an AM1.5G spectrum at 100 mW/cm^2 as measured by a certified oriel 91150 V calibration cell. A shadow mask was attached to each device prior to measurements to accurately define the corresponding device area. EQE measurements were performed by Newport System, Model 70356_70316NS. Atomic force microscopy (AFM) images were obtained using a Nanosurf easy scan two controller under the tapping mode. Electrochemical Impedance Spectroscopy (EIS) and Mott-Schottky measurements were performed using a Metrohm Autolab PGSTAT 302N, where for the EIS a red light-emitting diode (LED) (at 625 nm) was used as the light source calibrated to 100 mW/cm^2. For EIS a small AC perturbation of 20 mV was applied to the devices, and the different current output was measured throughout a frequency range of 1 MHz-1 Hz. The steady state DC bias was kept at 0 V throughout the EIS experiments. Mott-Schottky measurements on $FeMnO_3$ films were performed in a 0.5 M Na_2SO_4 aqueous electrolyte (pH = 7) using a Metrohm Autolab PGSTAT 302N potentiostat. A three-electrode set-up, with a platinum plate (1.0 × 2.0 cm^2) and a silver-silver chloride (Ag/AgCl, 3M KCl) as the counter and reference electrodes, respectively, was adopted to study the samples. The capacitance of the semiconductor/electrolyte interface was obtained at 1 kHz, with 10 mV AC voltage perturbation. All the experiments were conducted under dark conditions. The measured potential vs the Ag/AgCl reference electrode was converted to the normal hydrogen electrode (NHE) scale using the formula: $E_{NHE} = E_{Ag/AgCl} + 0.210$ V. The working electrode for impedance-potential measurement was fabricated as follows, 10 mg of $FeMnO_3$ NPs was dispersed in 1 ml DI water and the mixture was subjected to sonication in a water bath until a uniform suspension was formed. After that, 100 µl of the suspension was drop-casted onto the surface of fluorine-doped tin oxide (FTO, 9 Ω/sq) substrate, which was masked with an epoxy resin to expose an effective area of 1.0 × 1.0 cm^2. The sample was dried in a 60°C oven for 30 min.

RESULTS AND DISCUSSION

The solution processing technique provides an extensible low cost deposition procedure to fabricate high quality metal-oxide films and to replace costly and time consuming vacuum-deposition methods (Cochran et al., 2019). SCS has recently been employed in the low temperature manufacture of spinel nickel cobaltite ($NiCo_2O_4$) thin films as hole transport layers (HTLs) in inverted p-i-n perovskite solar cells (Papadas et al., 2018b). SCS possesses the benefit of speedily creating homogenous metal oxide materials of fine grain size. Most notably however, at a lower temperature than standard solid–state reaction, sol-gel and co-precipitation techniques (Chick et al., 1990; Rajeshwar and de Tacconi, 1998). Metal nitrates are distinguished for their capacity to synthesize metal oxides films of superior quality. Furthermore, it is important to choose the appropriate fuel agent for combustion, so as to circumvent the creation of sizeable clusters and particle agglomeration (Bansal, 2005; Verma et al., 2008). Tartaric acid was therefore used as the fuel agent in this work as it results in the formation of a single-crystalline phase of $FeMnO_3$. In general, tartaric acid leads to the formation of stable heterometallic polynuclear complexes (Selbach et al., 2007) because of its carboxylate and hydroxyl groups which can bind different metal ions from the solution, such as Mn^{2+} and Fe^{3+} (Wang et al., 2011). Basically, the growth of $FeMnO_3$ NPs is the result of combustion reaction of these polynuclear complexes while being heated in the presence of concentrated HNO_3 (Patil et al., 2002b; Cochran et al., 2019).

Synthesis and Characterization $FeMnO_3$ Nanoparticles

To achieve the solution combustion synthesis of $FeMnO_3$ NPs, tartaric acid and metal nitrates precursors were dissolved in 2-methoxyethanol. The precursor's solution was heated at 100°C under stirring until complete evaporation of the solvent. The obtained gel product was then analyzed by thermogravimetric analysis (TGA). The thermal behavior of the Mn/Fe-tartaric compound was observed by TGA, employing a heating rate of 10°C min^{-1} in ambient air. As illustrated in **Figure 1A**, the reaction shows an acute sudden mass loss at ~230°C, noted in TGA curve, which is associated with a strong exothermic release of energy during the combustion process. In our study, the as-synthesized material was crystallized well to the perovskite phase in ambient atmosphere at 450°C in a preheated oven for 6 h.

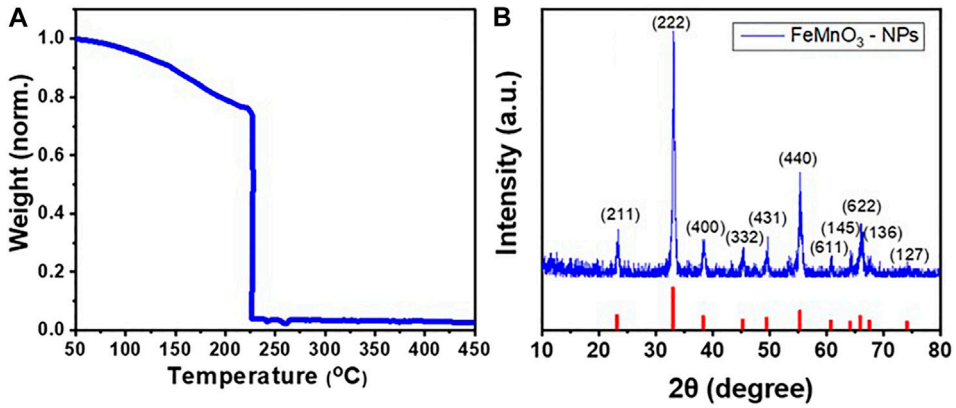

FIGURE 1 | (A) TGA profile of the as-prepared $FeMnO_3$ material synthesized via solution combustion process. The weight loss was normalized to the initial sample mass. **(B)** XRD pattern of $FeMnO_3$ NPs obtained at 450°C annealing temperature.

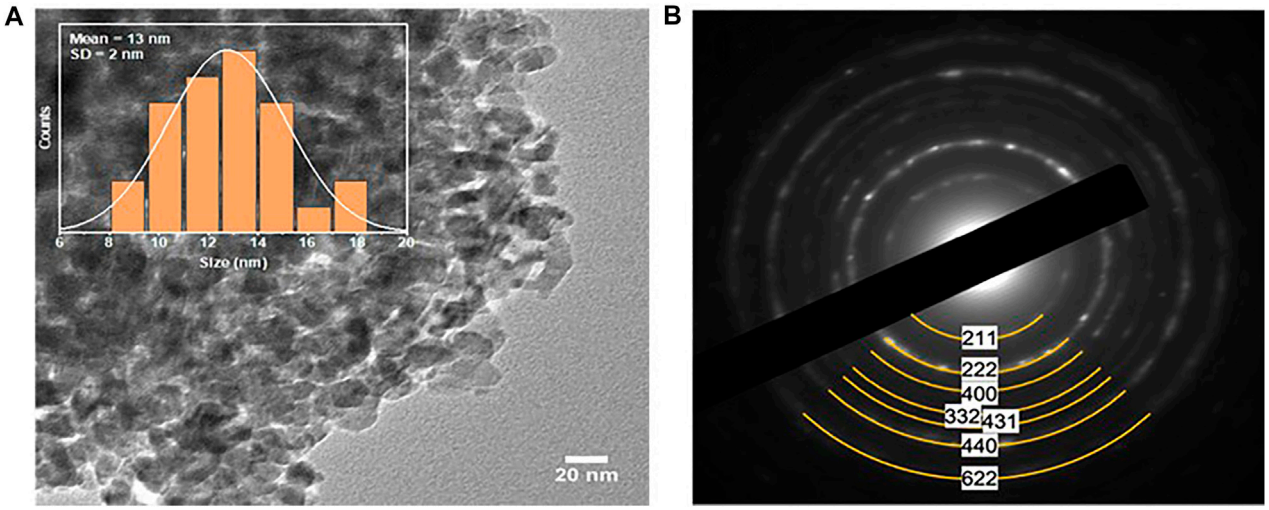

FIGURE 2 | (A) Representative TEM image (inset size distribution histogram of the $FeMnO_3$ NPs, showing an average diameter of 13 ± 2 nm), and **(B)** SAED pattern of the as-synthesized $FeMnO_3$ NPs obtained at 450°C.

The XRD measurement confirmed the crystallinity and phase purity of the $FeMnO_3$ NPs produced through the SCS method. **Figure 1B** depicts the XRD pattern of nanocrystalline $FeMnO_3$ obtained at 450°C soaking temperature. All the diffraction peaks compare well with the reported cubic iron manganite structure (JCPDS card #75–0,894) with a = b = c = 9.4 Å and α= β = γ = 90° unit cell parameters. No peaks from impurity phases, like MnO or Fe_2O_3, were observed in XRD pattern, showing the phase purity of the sample. The mean $FeMnO_3$ crystallite size is estimated at ~15 nm using the Scherrer`s equation and peak broadening of the (222) reflection.

TEM corroborated the phase purity of the obtained $FeMnO_3$ NPs. **Figure 2A** illustrates a characteristic TEM image of the $FeMnO_3$ sample fabricated at 450°C. It depicts that the obtained $FeMnO_3$ consists of tightly connected NPs with an average diameter of 13 ± 2 nm in average (inset **Figure 2A**), which match well to the crystallite size calculated from XRD. The crystal structure of the $FeMnO_3$ was then examined by selected-area electron diffraction (SAED). The SAED pattern recorded from a small area of the $FeMnO_3$ sample (**Figure 2B**) indicates a series of broad concentric diffraction rings, which can be assigned to the cubic phase of $FeMnO_3$ (Li et al., 2014). In line with XRD results, no other crystal phases were detected by means of electron diffraction. Furthermore, characterization of the composition of $FeMnO_3$ with EDS analysis revealed a Fe:Mn atomic ratio close to 1:1, in agreement with the stoichiometry of $FeMnO_3$ compound (**Supplementary Figure S1**).

The electronic structure of as-prepared $FeMnO_3$ was also examined by diffuse reflectance ultraviolet-visible/near-IR (UV-vis/NIR) spectroscopy. **Figure 3A** shows the UV-vis/NIR absorption spectrum for $FeMnO_3$ NPs synthesized at 450°C by SCS. This sample shows an acute optical absorption onset in the

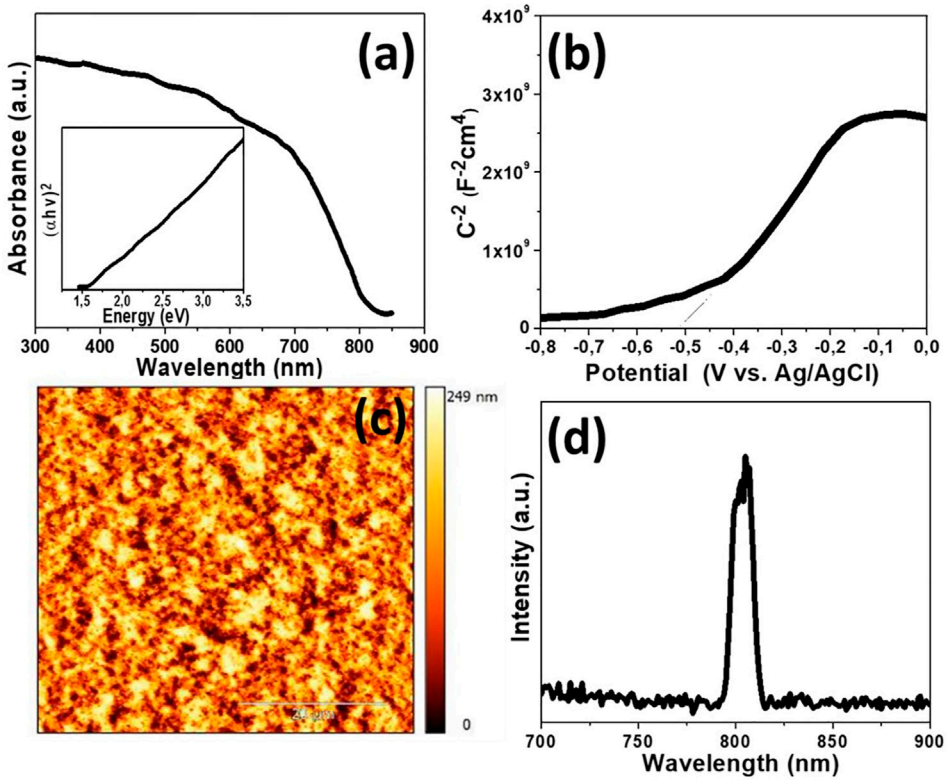

FIGURE 3 | (A) UV-Vis/NIR absorption spectrum of $FeMnO_3$ NPs [Inset: the $(Fhv)^2$ versus hv plot derived from optical absorption spectra]. **(B)** Mott-Schottky plot of the inverse square space-charge capacitance ($1/C_{SC}^2$) as a function of applied voltage (E) relative to the redox potential of Ag/AgCl (3 M KCl) for the $FeMnO_3$ NPs. **(C)** Typical AFM image of the ITO/$FeMnO_3$ film after SCS synthesis at 450°C (The scale bar is 20 μm). **(D)** Room-temperature PL emission spectra of the $FeMnO_3$ NPs.

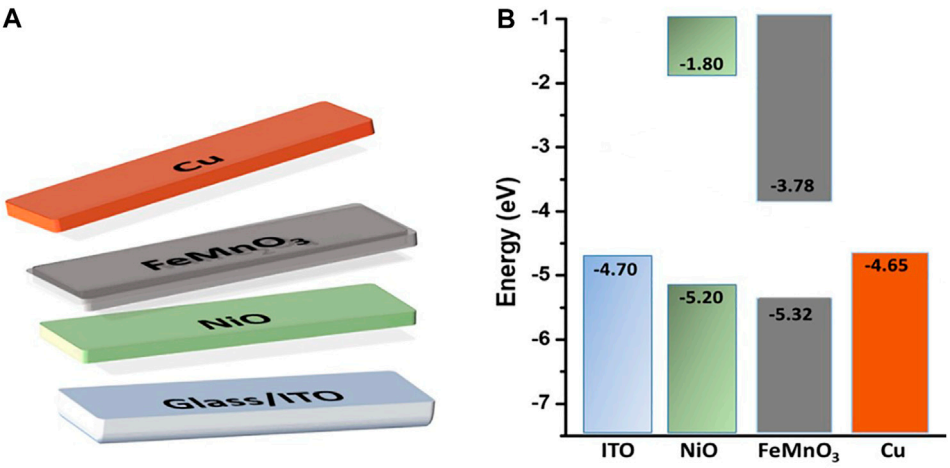

FIGURE 4 | (A) Schematic representation, and **(B)** the corresponding energy level diagram of each component of the ITO/NiO/$FeMnO_3$/Cu device.

near IR region (~805 nm), which is associated with an energy gap at ~1.54 eV, as determined by Tauc`s plots [$(Fhv)^{1/2}$ versus photon energy (hv), where F, h, and v are the Kubelka-Munk function of the reflectance, Plank constant and light frequency, respectively] (Kubelka, 1948), see inset of **Figure 3A**.

Electrochemical impedance spectroscopy (EIS) thereafter was employed to examine the position of the conduction band (CB) and valence band (VB) edges of $FeMnO_3$ material. **Figure 3B** shows the ensuing Mott-Schottky plot and the matching fit of the linear part of the inverse square space-charge capacitance ($1/C_{sc}^2$)

as a function of potential (E). The $FeMnO_3$ reveals a positive linear slope, showing n-type conductivity, where electrons are majority carriers. By using extrapolation to $1/C_{SC}^2 = 0$, the flat-band potential (E_{FB}) of $FeMnO_3$ NPs was estimated to be −0.31 eV vs. NHE (pH = 7). Based on the E_{FB} and optical bandgap (as obtained from UV-vis/NIR reflectance data, **Figure 3A**) values, the energy band edges for $FeMnO_3$ NPs are CB: 3.78 eV and VB: 5.32 eV vs. vacuum (Skliri, 2018). This is further highlighted in the energy level diagram shown in **Figure 4B**, which is based on EIS measured values for $FeMnO_3$ and literature data for ITO, NiO and Cu components (Haque et al., 2017). For heavily n-typed doped semiconductors, it can be supposed that the E_{FB} level is very close to the CB edge. Generally, for several n-type semiconductors the CB edge is approximately 0.1–0.3 eV higher than the E_{FB} potential. Therefore, the position of the VB edge was estimated from E_{FB}–E_g. In iron manganite materials there are a number of reports which connect the electron hopping between Fe^{+3}-Fe^{+2} and hole hopping between Mn^{+2}-Mn^{+3} ions with n-type and p-type of conductivities (Veena Gopalan et al., 2008; Batoo et al., 2009). The findings of these studies suggest that both n-type and p-type charge carriers are anticipated to contribute to the conduction mechanism in $FeMnO_3$ structure (Rezlescu and Rezlescu, 1974; Akhtar and Younas, 2012) In our study, the positive slope of the Mott-Schottky plots (**Figure 3B**) clearly shows that the perovskite iron manganite have n-type behavior (Skliri, 2018).

The smoothness of deposited $FeMnO_3$ film plays a crucial role for the formation of a deep depletion region, which is highly desirable for high performing devices. To achieve this β-alanine was used as surface capping ligand for $FeMnO_3$ NPs. During this process, the carboxyl ($-CO_2H$) groups of β-alanine adjust to the nanoparticle's surface, whereas the amine ($-NH_2$) functional groups inhibit the nanoparticles aggregation whilst stabilizing the colloidal solution. This resulted in the formation of a ~500 nm thick compact film (**Supplementary Figure S2**) consisting of a continuous network of tightly interconnected NPs (**Supplementary Figure S3**) with a relative low roughness of ~27 nm, as calculated by AFM topography measurements (**Figure 3C**).

For PL measurements of perovskite material, thick layers of $FeMnO_3$ NPs were manufactured on top of the quartz substrates utilizing the spin coating method (for details, see the experimental section). PL spectroscopy is an essential tool for finding the purity and crystalline quality of semiconductors. The PL spectrum of $FeMnO_3$ NPs, in **Figure 3D**, shows an intense near band edge emission at ~805 nm. This emission peak corresponds to the CB-VB inter-band transition and no additional peaks due to the radiative relaxations from defect sites or impurities were observed in PL spectrum of $FeMnO_3$ (Vasiljevic et al., 2020a).

Photovoltaic Device Characterization

As a proof of concept, the newly developed $FeMnO_3$ NP aggregates were used as a n-type photoactive material in a p-n full metal oxides solar cell, with the structure ITO/NiO/FMO/Cu (**Figure 4A**). Both NiO and $FeMnO_3$ materials were synthesized by the solution combustion method, as it is described in the experimental sections, rendering the fabrication process of such solar cells remarkably facile. Lastly, a 200-nm-thick Cu layer was thermally placed on the surface of $FeMnO_3$ to complete the device (see **Figure 4A**).

Figure 5A shows the J–V curve of the ITO/NiO/$FeMnO_3$/Cu device under 1 Sun simulated light (100 mW cm^{-2}) where the curve shape evidence the Schottky barrier formation at the junctions. The extracted photovoltaic parameters, open-circuit voltage (V_{oc}), short-circuit current (I_{sc}), fill factor (FF), and power conversion efficiency (PCE) are listed in **Table 1**. The device yields a high V_{oc} of 1.31 V with adequate FF of 54.3%, but the generated current density is low (J_{sc} = 0.07 mA cm^{-2}) delivering a PCE of 0.05%.

Among the studied all-oxide ferroic solar cells, that were fabricated by the same solution processes, the highest PCE was obtained by $FeMnO_3$-based solar cell (~0.05%), which is notably higher than those of the NiO/$BiFeO_3$ (~0.025%) (Chatterjee et al., 2014) and pure Pb(ZrTi)O_3 (~0.00008%) based solar cells (Paik et al., 2016). Furthermore, the obtained V_{oc} of the $FeMnO_3$-based solar cell (~1.31 V) is also much higher with respect to the solar cells using $BiFeO_3$ (~0.41 V) (Chatterjee et al., 2014) and Pb(ZrTi)O_3 (~0.6 V) as a light absorber, respectively (Paik et al., 2016). Consequently, we suggest that $FeMnO_3$ could be a potential candidate for solar cell applications.

To examine the spectral response of the device, external quantum efficiency (EQE) measurements were conducted, while the results being presented in **Figure 5B** along with the respective integrated photocurrent response. The spectral response of EQE reveals that the photo-generated current is produced in both NiO and $FeMnO_3$ layers with the spectrum correspondingly match the optical absorption spectra of the respective NiO and $FeMnO_3$ films. Specifically, we observe photocurrent generation onsets in the ultraviolent (300–350 nm) and near IR (800–850 nm) regions, which correspond to the acute optical absorption onset of NiO (~355 nm) and $FeMnO_3$ (~805 nm), respectively (Tang et al., 2018). Thus, in the device structure under investigation the p-type NiO provides a small contribution to the external quantum efficiency as discussed above and for this reason the term NiO/$FeMnO_3$-based heterojunction solar cells is used within the paper. The integrated photocurrent density (0.064 mA/cm^2) is also in close accord with the value obtained from the J–V curve (0.07 mA/cm^2) acquired from the solar simulator analysis.

EIS measurements were performed to obtain further insights into the depletion regions of the p–n device under study and to further understand the low generated photocurrent. Previous reported EIS measurements on lead free perovskite oxides have been performed at Voc conditions (Sariful Sheikh et al., 2017). Our trials to measure at Voc conditions resulted to low signal and high noise from moderate to high frequencies that do not enabled the analysis of EIS parameters. Thus, the presented measurements were performed under illumination and at Jsc conditions which provided adequate signal for the analysis of the EIS measurements. **Figure 5C**, shows characteristic Nyquist plots of the NiO/$FeMnO_3$ heterojunction structure as well as the equivalent circuit model used to fit the experimental data; Even though the model does not perfectly much the experimental results is used to provide initial analysis of the EIS measurements presented. Specifically, the model is commonly used with the components R_1, R_3 and R_3 being ascribed to the contacting, charge transport and recombination resistance, respectively (von Hauff, 2019). The obtained results shown in

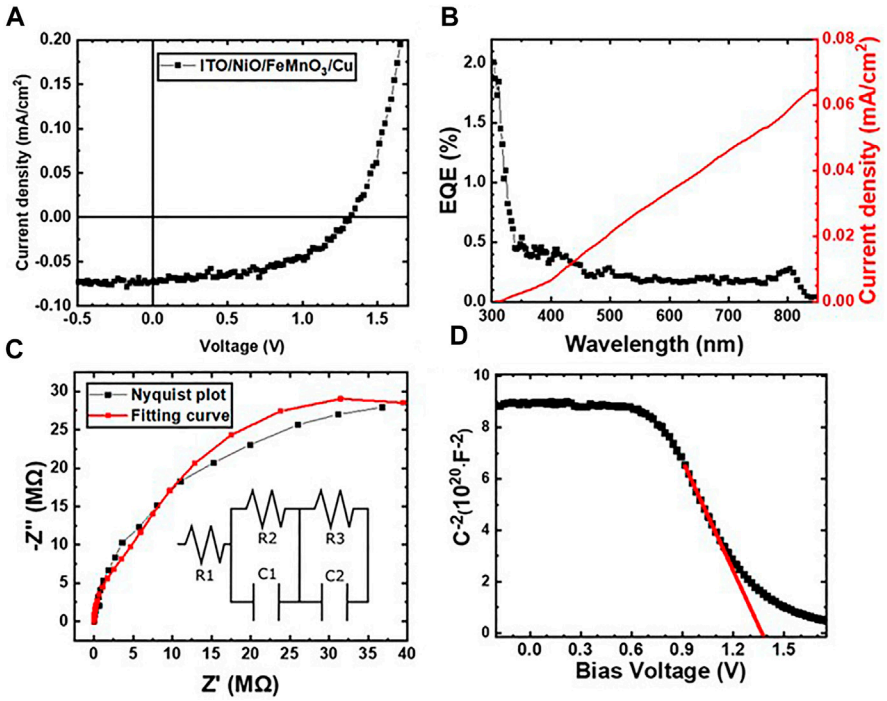

FIGURE 5 | (A) J-V plot under illumination conditions for the representative p-n device under this study ITO/NiO/$FeMnO_3$/Cu. **(B)** EQE spectrum of NiO–$FeMnO_3$ (p–n) heterojunction sandwiched between ITO and Cu electrodes. The right axis represents the integrated photocurrent density of the corresponding device. **(C)** Nyquist, and **(D)** Mott–Schottky plots for the ITO/NiO/$FeMnO_3$/Cu device.

TABLE 1 | Extracted solar cell parameters from the J–V characterization of the ITO/NiO/$FeMnO_3$/Cu device.

Solar cell	V_{oc} (V)	J_{sc} (mA/cm^2)	FF (%)	PCE (%)
ITO/NiO/FMO/Cu	1.31	0.07	54.3	0.05

TABLE 2 | Parameters obtained by fitting the Nyquist plots of the ITO/NiO/$FeMnO_3$/Cu device.

Solar cell	R_1 (KΩ)	R_2 (MΩ)	C_1 (nF)	R_3 (MΩ)	C_2 (nF)
ITO/NiO/FMO/Cu	1.83	5.52	0.053	57.27	0.059

Table 2 indicate that $R_3 > R_2$ by an order of magnitude and so we can infer that the ITO/NiO/$FeMnO_3$/Cu device exhibits a relative high recombination resistance which can explain the high V_{oc} value, but on the other hand shows a high charge transport resistance which results in limited current density. We note that the value of recombination resistance is expected to be lower at Voc conditions due to the absence of the depletion's layer driving force formed by the applied Jsc measuring conditions. In **Figure 5D**, the Mott-Schottky measurements of the title device which was swept from low to high external applied bias are illustrated. According to Mott-Schottky analysis the crossing of extrapolated linear section of the spectra with *x*-axis can be ascribed to the built-in potential of the device. Assuming that the proposed device is fully depleted during the measurement we exact a built-in potential of 1.38 V (von Hauff, 2019).

Overall, to achieve higher PCE from the presented solution processed NiO/$FeMnO_3$ heterojunction inorganic photovoltaics, further research and material development methods are needed. The main limiting factor that must be addressed is the improvement of n-type $FeMnO_3$ charge transport properties and thickness optimization of the active layer to decrease the charge carrier recombination. In parallel, incorporation of buffer layers within the ITO/NiO/$FeMnO_3$/Cu device structure can be used to improved charge carrier selectivity as well as a more appropriate p-type material can be applied with higher light harvesting capabilities and better aligned VB level edge to n-type $FeMnO_3$ to facilitate the holes transfer. The above proposed research and material development efforts can result to higher PCE for solution processed based heterojunction inorganic photovoltaics.

CONCLUSION

This study successfully proves that the synthesis of $FeMnO_3$ NPs can be achieved by a solution combustion technique, using tartaric acid as a fuel. Furthermore, the ultimate control of the nanoparticle's size can be readily attained due to the multiple binding ability of the tartaric acid that resulted in the formation of single-phase $FeMnO_3$ with an average particle size of 13 ± 2 nm. X-ray diffraction and electron microscopy measurements verified the high phase purity and crystallinity of $FeMnO_3$. Additionally, we used a method to construct a network of tightly connected $FeMnO_3$ nanoparticles by spin coating of the colloidal solution. In this study, β-alanine was

used as surface capping agent to produce a stable colloidal dispersion of $FeMnO_3$ NPs (β-alanine-capped $FeMnO_3$ NPs) in DMF. The short chain length of β-alanine allows direct interactions between the nanoparticles through ligand removal by thermal annealing (at 450°C in air), thus yielding a thick absorbing film (~500 nm) consisting of continuous layers of interconnected nanoparticles and exhibiting a relative low roughness of ~27 nm. The proposed strategy is crucial to obtain functional all-oxide photovoltaic devices that are developed using a process technique based on a simple solution. Furthermore, the inorganic perovskite $FeMnO_3$ was tested as a light absorber for photovoltaic applications for the first time. The band gap (~1.54 eV) of the synthesized $FeMnO_3$ nanostructure was found to be very close to the hybrid lead perovskite $CH_3NH_3PbI_3$ material (~1.55 eV). To this end, all-inorganic $NiO/FeMnO_3$ heterojunction photovoltaics were fabricated by solution combustion synthesis, using spin coating techniques. The corresponding all-inorganic solar cells reveal a high open circuit voltage (V_{oc}) of 1.31 V with a fill factor (FF) of 54.3% but exhibit a PCE of 0.05% under 100 mW cm^{-2} illumination due to the limited short circuit current 0.07 mA cm^{-2}. Electrical characterization by impedance spectroscopy showed that the $ITO/NiO/FeMnO_3/Cu$ device exhibits a high recombination resistance justifying the high V_{oc}. The high charge transport resistance indicates charge transport limitations within the relative thick (~500 nm) n-type $FeMnO_3$ active layer. Optimizing the active layer thickness and improving the charge carrier transport properties are the main limiting processes of the n-type $FeMnO_3$ which results in low J_{sc} values for the presented solution processed based heterojunction inorganic photovoltaics. Moreover, further PCE improvement could be achieved by the incorporation of suitable charge selective contacts within the solar cell device architecture and the replacement of NiO with a more appropriate p-type material. The obtained results encourage more intense research on solution processed and environmentally friendly inorganic solar cells with suitable opto-electronic properties and high photon to electron conversion efficiency.

DATA AVAILABILITY STATEMENT

The raw data supporting the conclusion of this article will be made available by the authors, without undue reservation.

AUTHOR CONTRIBUTIONS

IP, AI, and SC conceived the idea of the presented synthesis of controllable monodispersed FeMnO3 nanoparticles and examined it as n-type photoactive layer in all-inorganic NiO/FeMnO3 solution processed heterojunction photovoltaics. GA and IP design the nanoparticulate metal oxide materials. AI, PE, and SC designed the device experimental laboratory procedures. IP and IV performed the synthesis and material characterization studies. AI fabricated the devices, performed device characterization measurements and analyzed the device performance data under the supervision of SC and PE. All authors discussed the results and commented on the manuscript. SC supervised the project.

FUNDING

This research was funded by the European Research Council (ERC) under the European Union's Horizon 2020 research and innovation program (Grant agreement No 647311) and further supported from the academic yearly research activity internal Cyprus University of Technology budget.

SUPPLEMENTARY MATERIAL

The Supplementary Material for this article can be found online at: https://www.frontiersin.org/articles/10.3389/fchem.2021.754487/full#supplementary-material

REFERENCES

Cetin, A., Önal, A. M., and Esenturk, E. N., "Nanowires assembled from iron manganite nanoparticles : Synthesis , characterization , and investigation of electrocatalytic properties for water oxidation reaction," pp. 1–9, 2019, doi:10.1557/jmr.2019.215

Akhtar, M. J., and Younas, M. (2012). Structural and transport properties of nanocrystalline MnFe 2O 4 synthesized by co-precipitation method. *Solid State. Sci.* 14 (10), 1536–1542. doi:10.1016/j.solidstatesciences.2012.08.026

Alves, A., Bergmann, C. P., and Berutti, F. A. (2013). *Novel Synthesis and Characterization of Nanostructured Materials*. Berlin: Springer. 978-3-642-41275-2.

Bansal, N. P. (2005). "Combustion Synthesis of $Sm_{0.5}Sr_{0.5}CoO_{3-x}$ and $La_{0.6}Sr_{0.4}CoO_{3-x}$ Nanopowders for Solid Oxide Fuel Cell Cathodes," in Conference Sixth Pacific Rim Conference on Ceramic and Glass Technology sponsored by the American Ceramic Society - 2005 Maui, Hawaii: NASA/TM—2005-213897 Available at: http://gltrs.grc.nasa.gov/.

Batoo, K. M., Kumar, S., Lee, C. G., and Alimuddin, A. (2009). Study of dielectric and ac impedance properties of Ti doped Mn ferrites. *Curr. Appl. Phys.* 9 (6), 1397–1406. doi:10.1016/j.cap.2009.03.012

Bennet, J., Tholkappiyan, R., Vishista, K., Jaya, N. V., and Hamed, F. (2016). Attestation in self-propagating combustion approach of spinel AFe 2 O 4 (A = Co, Mg and Mn) complexes bearing mixed oxidation states: Magnetostructural properties. *Appl. Surf. Sci.* 383, 113–125. doi:10.1016/j.apsusc.2016.04.177

Bin, H., Yao, Z., Zhu, S., Zhu, C., Pan, H., Chen, Z., et al. (2017). A high-performance anode material based on FeMnO3/graphene composite. *J. Alloys Compd.* 695, 1223–1230. doi:10.1016/j.jallcom.2016.10.249

Buonsanti, R., Pick, T. E., Krins, N., Richardson, T. J., Helms, B. A., and Milliron, D. J. (2012). Assembly of ligand-stripped nanocrystals into precisely controlled mesoporous architectures. *Nano Lett.* 12 (7), 3872–3877. doi:10.1021/nl302206s

Calnan, S. (2014). Applications of oxide coatings in photovoltaic devices. *Coatings* 4 (1), 162–202. doi:10.3390/coatings4010162

Cao, K., Liu, H., Xu, X., Wang, Y., and Jiao, L., (2016). FeMnO3, "A high-performance Li-ion battery anode material. *Chem. Commun.* 52 (76), 11414–11417. doi:10.1039/c6cc04891a

Chatterjee, S., Bera, A., and Pal, A. J. (2014). p-i-n heterojunctions with BiFeO3 perovskite nanoparticles and p-and n-type oxides: Photovoltaic properties. *ACS Appl. Mater. Inter.* 6 (22), 20479–20486. doi:10.1021/am506066m

Chick, L. A., Pederson, L. R., Maupin, G. D., Bates, J. L., Thomas, L. E., and Exarhos, G. J. (1990). Glycine-nitrate combustion synthesis of oxide ceramic powders. *Mater. Lett.* 10 (1–2), 6–12. doi:10.1016/0167-577X(90)90003-5

Chrissanthopoulos, A., Baskoutas, S., Bouropoulos, N., Dracopoulos, V., Poulopoulos, P., and Yannopoulos, S. N. (2011). Synthesis and characterization of ZnO/NiO p-n heterojunctions: ZnO nanorods grown on

NiO thin film by thermal evaporation. *Photon. Nanostructures - Fundam. Appl.* 9 (2), 132–139. doi:10.1016/j.photonics.2010.11.002

Cochran, E. A., Woods, K. N., Johnson, D. W., Page, C. J., and Boettcher, S. W. (2019). Unique chemistries of metal-nitrate precursors to form metal-oxide thin films from solution: materials for electronic and energy applications. *J. Mater. Chem. A.* 7 (42), 24124–24149. doi:10.1039/C9TA07727H

Deganello, F., Marcì, G., and Deganello, G. (2009). Citrate-nitrate auto-combustion synthesis of perovskite-type nanopowders: A systematic approach. *J. Eur. Ceram. Soc.* 29 (3), 439–450. doi:10.1016/j.jeurceramsoc.2008.06.012

Doroftei, C., Dorin, P., Rezlescu, E., and Rezlescu, N. (2014). Composites: Part B Structural and catalytic characterization of nanostructured iron manganite. *Compos. PART B* 67, 179–182. doi:10.1016/j.compositesb.2014.07.005

Ellabban, O., Abu-Rub, H., and Blaabjerg, F. (2014). Renewable energy resources: Current status, future prospects and their enabling technology. *Renew. Sust. Energ. Rev.* 39, 748–764. Nov. 2014. doi:10.1016/j.rser.2014.07.113

Skliri, E., "Assembly and photochemical properties of mesoporous networks of spinel ferrite nanoparticles for environmental photocatalytic remediation," *Appl. Catal. B Environ.*, vol. 227, no. pp. 330–339. 2018, doi:10.1016/j.apcatb.2018.01.045

Fix, T. (2019). *Oxide and Ferroelectric Solar Cells*. Amsterdam. Elsevier.

Fu, Q., Tang, X., Huang, B., Hu, T., Tan, L., Chen, L., et al. (2018387May 2018). Recent Progress on the Long-Term Stability of Perovskite Solar Cells. *Adv. Sci.* 5 (5), 1700387. doi:10.1002/advs.201700387

Galatopoulos, F., Savva, A., Papadas, I. T., and Choulis, S. A. (2017). The effect of hole transporting layer in charge accumulation properties of p-i-n perovskite solar cells. *APL Mater.* 5 (7), 076102. doi:10.1063/1.4991030

Gowreesan, S., and Ruban Kumar, A. (2017). Structural, magnetic, and electrical property of nanocrystalline perovskite structure of iron manganite (FeMnO3). *Appl. Phys. A. Mater. Sci. Process.* 123 (11), 1–8. doi:10.1007/s00339-017-1302-x

Grinberg, I., West, D. V., Torres, M., Gou, G., Stein, D. M., Wu, L., et al. (2013). Perovskite oxides for visible-light-absorbing ferroelectric and photovoltaic materials. *Nature* 503 (7477), 509–512. Nov. doi:10.1038/nature12622

Habibi, M. H., and Mosavi, V. (2017). Urea combustion synthesis of nano-structure bimetallic perovskite FeMnO3 and mixed monometallic iron manganese oxides: effects of preparation parameters on structural, opto-electronic and photocatalytic activity for photo-degradation of Basic Blue 12. *J. Mater. Sci. Mater. Electron.* 28 (12), 8473–8479. doi:10.1007/s10854-017-6568-4

Han, C.-H., Han, S.-D., Gwak, J., and Khatkar, S. P. (2007). Synthesis of indium tin oxide (ITO) and fluorine-doped tin oxide (FTO) nano-powder by sol-gel combustion hybrid method. *Mater. Lett.* 61 (8–9), 1701–1703. Apr. 2007. doi:10.1016/j.matlet.2006.07.114

Haque, M. A., Sheikh, A. D., Guan, X., and Wu, T. (2017). Metal Oxides as Efficient Charge Transporters in Perovskite Solar Cells. *Adv. Energ. Mater.* 7 (20), 1602803. doi:10.1002/aenm.201602803

Hsieh, H. H. (2014). Novel approaches for fabricating high-performance low-temperature solution-processed metal oxide transistors. *Dig. Tech. Pap. - SID Int. Symp.* 45 (1), 427–430. doi:10.1002/j.2168-0159.2014.tb00115.x

Hussein, A. K. (2015). Applications of nanotechnology in renewable energies-A comprehensive overview and understanding. *Renew. Sust. Energ. Rev.* 42, 460–476. doi:10.1016/j.rser.2014.10.027

Ioakeimidis, A., Papadas, I. T., Tsikritzis, D., Armatas, G. S., Kennou, S., and Choulis, S. A. (2019). Enhanced photovoltaic performance of perovskite solar cells by Co-doped spinel nickel cobaltite hole transporting layer. *APL Mater.* 7 (2), 021101. doi:10.1063/1.5079954

Jadhav, L. D., Patil, S. P., Chavan, A. U., Jamale, A. P., and Puri, V. R. (2011). Solution combustion synthesis of Cu nanoparticles: a role of oxidant-to-fuel ratio. *Micro Nano Lett.* 6 (9), 812–815. doi:10.1049/mnl.2011.0372

Jiang, Q., Lu, J., Cheng, J., Li, X., Sun, R., Feng, L., et al. (2014). Combustion-process derived comparable performances of Zn-(In:Sn)-O thin-film transistors with a complete miscibility. *Appl. Phys. Lett.* 105 (13), 132105. doi:10.1063/1.4896990

Jung, E. H., Jeon, N. J., Park, E. Y., Moon, C. S., Shin, T. J., Yang, T.-Y., et al. (2019). Efficient, stable and scalable perovskite solar cells using poly(3-hexylthiophene). *NatureMar* 567 (7749), 511–515. doi:10.1038/s41586-019-1036-3

Karsthof, R., Räcke, P., Von Wenckstern, H., and Grundmann, M. (2016). Semi-transparent NiO/ZnO UV photovoltaic cells. *Phys. Status Solidi Appl. Mater. Sci.* 213 (1), 30–37. doi:10.1002/pssa.201532625

Kawade, D., Moriyama, K., Nakamura, F., Chichibu, S. F., and Sugiyama, M. (2015). Fabrication of visible-light transparent solar cells composed of NiO/NixZn1-xO/ZnO heterostructures. *Phys. Status Solidi Curr. Top. Solid State. Phys.* 12 (6), 785–788. doi:10.1002/pssc.201400256

Kerli, S., and Alver, U. (2016). Preparation and characterisation of ZnO/NiO nanocomposite particles for solar cell applications. *J. Nanotechnol.* 2016. doi:10.1155/2016/4028062

Kim, H., Gilmore, C. M., Piqué, A., Horwitz, J. S., Mattoussi, H., Murata, H., et al. (1999). Electrical, optical, and structural properties of indium-tin-oxide thin films for organic light-emitting devices. *J. Appl. Phys.* 86 (11), 6451–6461. doi:10.1063/1.371708

Kim, M.-G., Kanatzidis, M. G., and Facchetti, A., (2011). Marks, "Low-temperature fabrication of high-performance metal oxide thin-film electronics via combustion processing SI. *Nat. Mater.* 10 (5), 382–388. doi:10.1038/nmat3011

Kosten, E. D., Atwater, J. H., Parsons, J., Polman, A., and Atwater, H. A. (2013). Highly efficient GaAs solar cells by limiting light emission angle. *Light Sci. Appl.* 2 (1), e45. doi:10.1038/lsa.2013.1

Kubelka, P. (1948). New Contributions to the Optics of Intensely Light-Scattering Materials Part I. *J. Opt. Soc. Am.* 38 (5), 448. doi:10.1364/JOSA.38.000448

Li, F., and Liu, M. (2017). Recent efficient strategies for improving the moisture stability of perovskite solar cells. *J. Mater. Chem. A.* 5 (30), 15447–15459. doi:10.1039/C7TA01325F

Li, M., Xu, W., Wang, W., Liu, Y., Cui, B., and Guo, X. (2014). Facile synthesis of specific FeMnO3 hollow sphere/graphene composites and their superior electrochemical energy storage performances for supercapacitor. *J. Power Sourc.* 248, 465–473. doi:10.1016/j.jpowsour.2013.09.075

Lobo, L. S., and Rubankumar, A. (2019). Investigation on structural and electrical properties of FeMnO 3 synthesized by sol-gel method. *Ionics (Kiel).* 25 (3), 1341–1350. doi:10.1007/s11581-018-2776-z

Mahmood, T., Saddique, M. T., Naeem, A., Westerhoff, P., Mustafa, S., and Alum, A. (2011). Comparison of Different Methods for the Point of Zero Charge Determination of NiO. *Ind. Eng. Chem. Res.* 50 (17), 10017–10023. doi:10.1021/ie200271d

Mimani, T., and Patil, K. C. (2001). Solution Combustion Synthesis of Nanoscale Oxides and Their Composites. *Mater. Phys. Mech.* 4, 134–137. doi:10.1016/j.materresbull.2008.09.034

Mitzi, D. B., Gunawan, O., Todorov, T. K., Wang, K., and Guha, S. (2011). The path towards a high-performance solution-processed kesterite solar cell. *Solar Energ. Mater. Solar Cell* 95 (6), 1421–1436. Jun. 2011. doi:10.1016/j.solmat.2010.11.028

Patel, M., "Excitonic metal oxide heterojunction (NiO/ZnO) solar cells for all-transparent module integration," *Sol. Energ. Mater. Sol. Cell*, vol. 170, no. June, pp. 246–253. 2017. doi:10.1016/j.solmat.2017.06.006

Sariful Sheikh, M., Ghosh, D., Dutta, A., Bhattacharyya, S., and Sinha, T. P., "Lead free double perovskite oxides Ln2NiMnO6 (Ln = La, Eu, Dy, Lu), a new promising material for photovoltaic application," *Mater. Sci. Eng. B Solid-state Mater. Adv. Technol.*, vol. 226, no. pp. 10–17. 2017. doi:10.1016/j.mseb.2017.08.027

Mungse, P. B., Saravanan, G., Nishibori, M., and Subrt, J. (2017). "Solvent-Free, Improved Synthesis of Pure Bixbyite Phase of Iron and Manganese Mixed Oxides as Low-cost, Potential Oxygen Carrier for Chemical Looping with Oxygen Uncoupling," in Conference 12th Conference on Solid State Chemistry - 2016, Prague, Czech Republic. doi:10.1515/pac-2016-1127

Nikolic, M. V., Krstic, J. B., Labus, N. J., Lukovic, M. D., Dojcinovic, M. P., Radovanovic, M., et al. "Structural, morphological and textural properties of iron manganite (FeMnO3) thick films applied for humidity sensing," *Mater. Sci. Eng. B Solid-state Mater. Adv. Technol.*, vol. 257, no, p. 114547, 2020, doi:10.1016/j.mseb.2020.114547

Nechache, R., Harnagea, C., Li, S., Cardenas, L., Huang, W., Chakrabartty, J., et al. (2014). Bandgap tuning of multiferroic oxide solar cells. *Nat. Photon* 9 (1), 61–67. doi:10.1038/nphoton.2014.255

Paik, Y. H., Kojori, H. S., Yun, J.-H., and Kim, S. J. (2016). Improved efficiency of ferroelectric Pb(Zr, Ti)O3 (PZT) based photovoltaic device with colloidal quantum dots. *Mater. Lett.* 185, 247–251. doi:10.1016/j.matlet.2016.08.082

Papadas, I., Christodoulides, J. A., Kioseoglou, G., and Armatas, G. S. (2015). A high surface area ordered mesoporous BiFeO3 semiconductor with efficient water oxidation activity. *J. Mater. Chem. A.* 3 (4), 1587–1593. doi:10.1039/C4TA05272B

Papadas, I. T., Galatopoulos, F., Armatas, G. S., Tessler, N., and Choulis, S. A. (2019). Nanoparticulate Metal Oxide Top Electrode Interface Modification

Improves the Thermal Stability of Inverted Perovskite Photovoltaics. *Nanomaterials* 9 (11), 1616, 2019 . Nov. doi:10.3390/nano9111616

Papadas, I. T., Ioakeimidis, A., Armatas, G. S., and Choulis, S. A. (2018). Low-Temperature Combustion Synthesis of a Spinel NiCo2 O4 Hole Transport Layer for Perovskite Photovoltaics. *Adv. Sci.* 5 (5), 1701029–9. doi:10.1002/advs.201701029

Papadas, I. T., Savva, A., Ioakeimidis, A., Eleftheriou, P., Armatas, G. S., and Choulis, S. A. (2018). Employing surfactant-assisted hydrothermal synthesis to control CuGaO2 nanoparticle formation and improved carrier selectivity of perovskite solar cells. *Mater. Today Energ.* 8, 57–64. doi:10.1016/j.mtener.2018.03.003

Papadas, I. T., Subrahmanyam, K. S., Kanatzidis, M. G., and Armatas, G. S. (2015). Templated assembly of BiFeO 3 nanocrystals into 3D mesoporous networks for catalytic applications. *Nanoscale* 7 (13), 5737–5743. doi:10.1039/C5NR00185D

Patil, K. C., Aruna, S. T., and Mimani, T. (2002). Combustion synthesis: An update. *Curr. Opin. Solid State. Mater. Sci.* 6 (6), 507–512. doi:10.1016/S1359-0286(02)00123-7

Patil, K. C., Aruna, S. T., and Mimani, T. (2002). Combustion synthesis: An update. *Curr. Opin. Solid State. Mater. Sci.* 6 (6), 507–512. doi:10.1016/S1359-0286(02)00123-7

Pérez-Tomás, A., Mingorance, A., Tanenbaum, D., and Lira-Cantú, M. (2018). *Metal Oxides in Photovoltaics: All-Oxide, Ferroic, and Perovskite Solar Cells*. Amsterdam: Elsevier.

Pérez-Tomas, A., Xie, H., Wang, Z., Kim, H.-S., Shirley, I., Turren-Cruz, S.-H., et al. (2019). PbZrTiO3 ferroelectric oxide as an electron extraction material for stable halide perovskite solar cells. *Sust. Energ. Fuels* 3 (2), 382–389. doi:10.1039/c8se00451j

Rajeshwar, K., and de Tacconi, N. R. (1998). Solution combustion synthesis of oxide semiconductors for solar energy conversion and environmental remediation. *Chem. Soc. Rev.* 38 (7), 1984. doi:10.1039/b811238j

Rezlescu, N., and Rezlescu, E. (1974). Dielectric properties of copper containing ferrites. *Phys. Status Solidi* 23 (2), 575–582. doi:10.1002/pssa.2210230229

Rohatgi, A. (1996). "Record high 18.6% efficient solar cell on HEM multicrystalline material," in *Conference Record of the Twenty Fifth IEEE Photovoltaic Specialists Conference - 1996* (New Jersey, 741–744. doi:10.1109/PVSC.1996.564236

Saravanakumar, B., Ramachandran, S. P., Ravi, G., Ganesh, V., Guduru, Ramesh. K., and Yuvakkumar, R. (2018). Electrochemical characterization of FeMnO3 microspheres as potential material for energy storage applications. *Mater. Res. Express* 5, 015504. doi:10.1088/2053-1591/aaa3b1

Savva, A., Papadas, I., Tsikritzis, D., Armatas, G. S., Kennou, S., and Choulis, S. (2017). Room Temperature Nanoparticulate Interfacial Layers for Perovskite Solar Cells via Solvothermal Synthesis. *J. Mater. Chem. A.* 5, 20381–20389. doi:10.1039/C7TA03802J

Selbach, S. M., Einarsrud, M.-A., Tybell, T., and Grande, T. (2007). Synthesis of BiFeO $_3$ by Wet Chemical Methods. *J. Am. Ceram. Soc.* 90 (11), 3430–3434. doi:10.1111/j.1551-2916.2007.01937.x

Seo, J.-Y., Uchida, R., Kim, H.-S., Saygili, Y., Luo, J., Moore, C., et al. (2018). Boosting the Efficiency of Perovskite Solar Cells with CsBr-Modified Mesoporous TiO2 Beads as Electron-Selective Contact. *Adv. Funct. Mater.* 28 (15), 1705763. doi:10.1002/adfm.201705763

Shin, S. S., Lee, S. J., and Seok, S. I. (2019). Exploring wide bandgap metal oxides for perovskite solar cells. *APL Mater.* 7 (2), 022401. doi:10.1063/1.5055607

Soni, D., and Pal, R. (2016). Nanocrystalline Manganese Iron Oxide as a C,harge Storage Electrode. *Electroanalysis* 28 (9), 1951–1956. doi:10.1002/elan.201600031

Sun, Y., Guo, F., Chen, J., and Zhao, S. (2017). Improved ferroelectric and photovoltaic properties of BiMnO3 modified lead-free K0.5Na0.5NbO3 solid-solution films. *Appl. Phys. Lett.* 111 (25), 253901. doi:10.1063/1.5006643

Sundari, R., Hua, T. I., and Rusli Yosfiah, M. (2013). Effect of calcinations on characterizations of fabricated nano manganese ferrite. *Adv. Mater. Res.* 634 (1), 2150–2154. doi:10.4028/www.scientific.net/AMR.634-638.2150

Suresh, K., Kumar, N. R. S., and Patil, K. C. (1991). A novel combustion synthesis of spinel ferrites, orthoferrites and garnets. *Adv. Mater.*, 3, 148–150. doi:10.1002/adma.19910030306

Tang, L. J., Chen, X., Wen, T. Y., Yang, S., Zhao, J. J., Qiao, H. W., et al. (2018). A Solution-Processed Transparent NiO Hole-Extraction Layer for High-Performance Inverted Perovskite Solar Cells. *Chem. - A. Eur. J.* 24 (12), 2845–2849. doi:10.1002/chem.201705658

Ukoba, K. O., Inambao, F. L., and Eloka-Eboka, A. C. (2018). Fabrication of affordable and sustainable solar cells using NiO/TiO2 P-N heterojunction. *Int. J. Photoenergy* 2018. doi:10.1155/2018/6062390

Vasiljevic, Z. Z., Dojcinovic, M. P., Krstic, J. B., and Ribic, V. (2020). Synthesis and antibacterial activity of iron manganite (FeMnO3) particles against the environmental bacterium Bacillus subtilis. *Bacillus subtilis*, 13879, 2020 . 13888. doi:10.1039/d0ra01809k

Vasiljevic, Z. Z., Dojcinovic, M. P., Krstic, J. B., Ribic, V., Tadic, N. B., Ognjanovic, M., et al. (2020). Synthesis and antibacterial activity of iron manganite (FeMnO3) particles against the environmental bacterium: Bacillus subtilis. *RSC Adv.* 10 (23), 13879–13888. doi:10.1039/d0ra01809k

Veena Gopalan, E., Malini, K. A., Saravanan, S., Sakthi Kumar, D., Yoshida, Y., and Anantharaman, M. R. (2008). Evidence for polaron conduction in nanostructured manganese ferrite. *J. Phys. D. Appl. Phys.* 41 (18), 185005. doi:10.1088/0022-3727/41/18/185005

Verma, S., Joshi, H. M., Jagadale, T., Chawla, A., Chandra, R., and Ogale, S. (2008). Nearly Monodispersed Multifunctional NiCo 2 O 4 Spinel Nanoparticles: Magnetism, Infrared Transparency, and Radiofrequency Absorption. *J. Phys. Chem. C* 112 (39), 15106–15112. doi:10.1021/jp804923t

von Hauff, E. (2019). Impedance Spectroscopy for Emerging Photovoltaics. *J. Phys. Chem. C* 123 (18), 11329–11346. doi:10.1021/acs.jpcc.9b00892

Wang, W. (2014). Device characteristics of CZTSSe thin-film solar cells with 12.6% efficiency. *Adv. Energ. Mater.* 4 (7), 1–5. doi:10.1002/aenm.201301465

Wang, Y., Hu, Y., Fei, L., Zhang, Y., Yuan, J., and Gu, H. (2011). Synthesis of bismuth ferrite nanoparticles via a wet chemical route at low temperature. *J. Nanomater.* 2011. doi:10.1155/2011/797639

Warasawa, M., Watanabe, Y., Ishida, J., Murata, Y., Chichibu, S. F., and Sugiyama, M. (2013). Fabrication of visible-light-transparent solar cells using p-type nio films by low oxygen fraction reactive rf sputtering deposition. *Jpn. J. Appl. Phys.* 52 (2). doi:10.7567/JJAP.52.021102

Xiong, L., Guo, Y., Wen, J., Liu, H., Yang, G., Qin, P., et al. (2018). Review on the Application of SnO2 in Perovskite Solar Cells. *Adv. Funct. Mater.* 28 (35), 1802757. doi:10.1002/adfm.201802757

Yu, X. (2015). Spray-combustion synthesis: efficient solution route to high-performance oxide transistors. *Proc. Natl. Acad. Sci. U. S. A.* 112 (11), 3217–3222. doi:10.1073/pnas.1501548112

Zhang, G., Wu, H., Li, G., Huang, Q., Yang, C., Huang, F., et al. (2013). New high Tc multiferroics KBiFe2O5 with narrow band gap and promising photovoltaic effect. *Sci. Rep.* 3 (1), 1265. doi:10.1038/srep01265

Zhang, H. (2015). Pinhole-Free and Surface-Nanostructured NiOx Film by Room-Temperature Solution Process for High-Performance Flexible Perovskite Solar Cells with Good Stability and Reproducibility. *ACS Nano*, acsnano.5b07043. doi:10.1021/acsnano.5b07043

Conflict of Interest: The authors declare that the research was conducted in the absence of any commercial or financial relationships that could be construed as a potential conflict of interest.

Publisher's Note: All claims expressed in this article are solely those of the authors and do not necessarily represent those of their affiliated organizations, or those of the publisher, the editors and the reviewers. Any product that may be evaluated in this article, or claim that may be made by its manufacturer, is not guaranteed or endorsed by the publisher.